Journal of Atmospheric and Solar–Terrestrial Physics 282 (2026) 106805

Contents lists available at ScienceDirect

Journal of Atmospheric and Solar–Terrestrial Physics

journal homepage: www.elsevier.com/locate/jastp

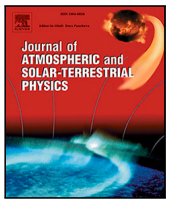

Research Paper

Extreme scintillation structure diagnostics

Charles Rino [a,*], Charles Carrano [a], Dmytro Vasylyev [c], Luca Spogli [d], Theodore Beach [a], Yu Morton [b], Keith Groves [a]

[a] Institute for Scientific Research, Boston College, MA, USA
[b] University of Colorado, Boulder, CO, USA
[c] Institute for Solar-Terrestrial Physics, German Aerospace Center, Neustrelitz, Germany
[d] Istituto Nazionale di Geofisica e Vulcanologia, Rome, Italy

ARTICLE INFO

Keywords:
Ionosphere
GNSS scintillation
Equatorial plasma bubbles
Backpropagation

ABSTRACT

Satellite constellations that comprise the global navigation satellite system are monitoring the ionosphere routinely for space-weather forecasting. However, quantitative statistical characterization of ionospheric irregularities has been confined to dedicated studies. This paper demonstrates and validates a new diagnostic procedure that exploits back propagation (BP) to reduce diffraction that develops as signals propagate through disturbed ionosphere regions and ensuing free space. BP has been used primarily to localize structure imparted to ionosphere occultation measurements. However, BP can be applied more broadly to satellite-to-near-earth observations. The new approach applies irregularity parameter estimation (IPE) to phase extracted after BP.

BP-IPE applications to low-latitude strong scintillation data are presented, which reveal new irregularity characteristics distinctly different from commonly measured characteristics associated with equatorial plasma bubbles. The procedures are validated with multiple phase screen simulations.

1. Introduction

Scintillation observed on satellite signals that have traversed the earth's ionosphere is caused by stochastic electron density structure intercepted as the signals propagate from a source to a receiver. Stochastic electron density structure is characterized by a 3D spectral density function (SDF), which is defined as the average intensity of a 3D spatial Fourier decomposition of the structure. As will be described in more detail in the development, observable manifestations of the electron density structure are characterized by path-integrated electron density scaled to phase units. The phase power spectral density (PSD) of a translating path-integrated phase time series, $\phi(t)$, is typically assigned an inverse power law form

$$\Phi_\phi(f) \propto |f|^{-p}, \tag{1}$$

where f is frequency offset from the carrier frequency. From early rocket measurements of scintillation associated with electron density structures described graphically as equatorial plasma bubbles (EPBs) (Rino et al., 1981), the more detailed two-component power-law form

$$\Phi_\phi(f) = C_P \begin{cases} |f|^{-p_1}, & \text{for } |f| \le f_0 \\ f_0^{p_2-p_1}|f|^{-p_2}, & \text{for } |f| > f_0 \end{cases}, \tag{2}$$

was introduced. To the extent that an estimate of the path-integrated phase can be constructed, a formal irregularity parameter estimation (IPE) procedure can be applied to the measured phase PSD to estimate the parameters, C_P, p_1, p_2, and f_0, which characterize the phase structure. The challenge is to overcome diffraction effects that distort the signal phase from the path-integrated form that supports diagnostic structure characterization.

The initial objective of the research reported in this paper was to demonstrate and validate a new diagnostic procedure that exploits back propagation (BP) to mitigate diffraction effects. It is well known that BP can remove or reduce scintillation. However, BP scintillation minimization has been used mainly to estimate the occultation path location of the intercepted stochastic structure (Ludwig-Barbosa et al., 2023). With conventional satellite-to-earth geometries the ionosphere penetration point at a specified height provides an estimate of the location of the disturbed region. The BP reduction of scintillation itself can be exploited for typically intercepted structure regions. Breitsch et al. (2020) used BP scintillation reduction to improve phase tracking. Following Breitsch and Morton, we applied IPE to the phase extracted from the BP field.

Upon validating the BP-IPE procedure with multiple-phase-screen (MPS) simulations, BP-IPE was applied to a large number of disturbed equatorial (Global Positioning System) GPS passes collected at a low-latitude Hong Kong station from October 2013 to July 2015.

* Corresponding author.
E-mail addresses: crino@comcast.net, rino@bc.edu (C. Rino).

https://doi.org/10.1016/j.jastp.2026.106805
Received 27 October 2025; Received in revised form 20 March 2026; Accepted 4 April 2026
Available online 6 April 2026

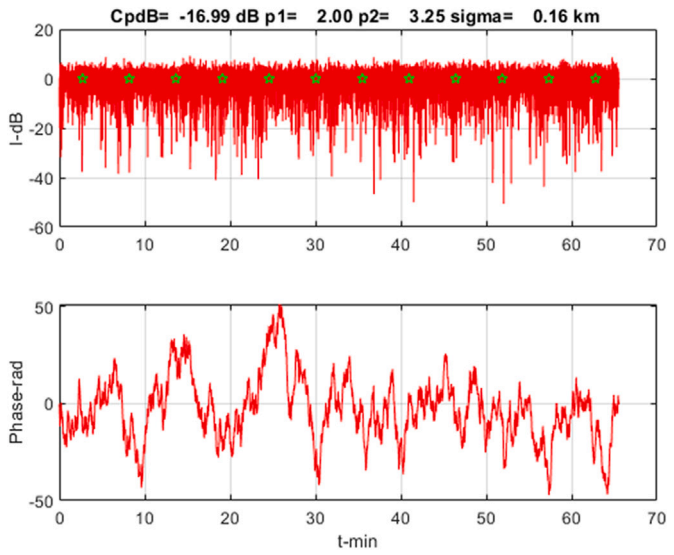

Fig. 1. The upper frame shows the simulated EPB intensity at 142 km. The lower frame shows the extracted phase. Green pentagrams locate 5-min segment centers.

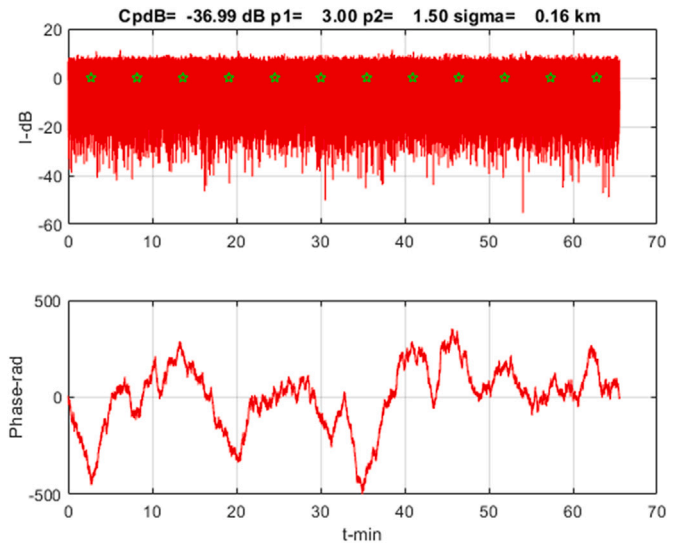

Fig. 2. The upper frame shows the simulated PPB intensity at 142 km. The lower frame shows the extracted phase. Green pentagrams locate 5-min segment centers.

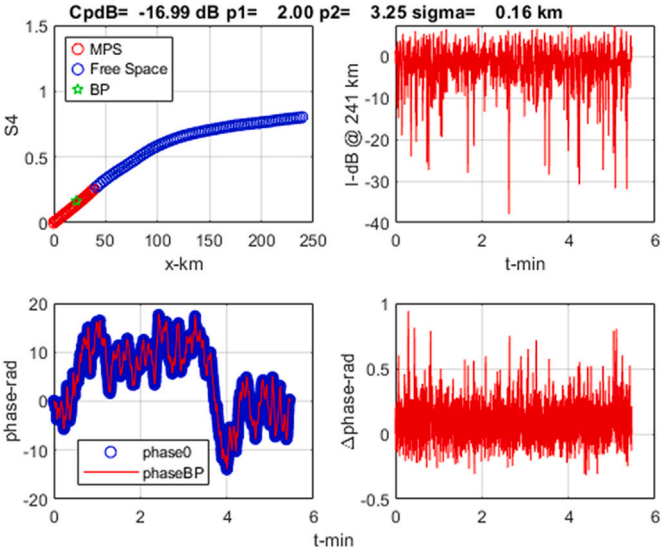

Fig. 3. EPB segment 1 summary: The upper left frame shows the MPS $S4$ evolution (red) and the subsequent free-space evolution(blue). The green pentagram identifies the BP range and $S4$. The upper right frame repeats the intensity at 142 km for reference. The lower left frame compares the initiating and BP-recovered phase. The lower right frame shows the phase difference.

As summarized in Section 4, whereas most of the in-situ and remote diagnostics of scintillation associated with EPBs have reported SDFs with $p_1 < p_2$, we found that more than 50% of the Hong Kong data segments had SDFs with $p_1 > p_2$. We believe this finding is indicative of a new stochastic structure class, which we identified as pronounced plasma bubble (PPB) referring to the enhancement of the large-scale structure implied by the larger p_1 value. The simulations used to validate the BP-IPE diagnostics were chosen to be representative of the EPB and PPB structure classes. The remainder of this paper summarizes the BP-IPE analysis and MPS validation, followed by a summary of the BP-IPE applications to Hong Kong data and more recent Global Navigation Satellite System (GNSS) data, which include results from the May 10 Gannon Storm.

As summarized in Section 2, diagnostic processing starts with a 3D statistical model of stochastic electron density structure. The stochastic structure of interest, which is referred to herein as intermediate scale structure, spans tens of kilometers to hundreds of meters. The analytic form (3) is defined by four parameters, namely C_s, η_1, η_2, and κ_0. For propagation in planes that cut across elongated field-aligned structure, two-dimensional propagation captures the defining structure. The one-dimensional integral in (4) is a measure of total electron content (TEC). Scaling the result to frequency-dependent phase units represents the ideal phase extracted by GNSS processors. Expressing results in spatial units rather than the measured temporal units assumes structure invariance over the measurement interval, whereby the path motion and direction relative to the magnetic field are sufficient to convert measured time series to projected spatial measures. Additional assumptions involving correlation over the propagation path lead to (8) with C_p, p_1, p_2, and κ_0 identified as equivalent spatial-Fourier-domain parameters that characterize the stochastic structure.

Following the summary of the structure model and critical assumptions, Section 2 describes the BP-IPE procedure, which requires only standard Fourier analysis embedded in a standard minimization procedure. Section 3 summarizes the BP-IPE validation. Figs. 1 and 2 show, respectively, representative EPB and PPB realizations. Figs. 3 and 4 illustrate the BP recovery of the initiating path-integrated phase structure. Figs. 5 and 6 summarize the similarly behaved IPE parameters derived from the representative IPE and PPB simulations. Fig. 10 summarizes the EPB and PPB classes identified in Hong Kong data, which can be compared to the representative simulations shown in Figs. 3 and 4. Figs. 14 and 15 summarize the results of applying the BP-IPE analysis to the more recent GNSS data, which show small numbers of EPB structure segments. For a first reading the detailed description and validation of the BP-IPE procedures in Section 2 can be skipped.

2. BP diagnostic processing

Diagnostic processing starts with a parameterized 3D structure model. The 3D SDF model

$$\Phi_{\Delta N_e}(\kappa_s) = C_s \begin{cases} \kappa_s^{-\eta_1}, & \kappa_s \leq \kappa_0 \\ (\kappa_0^{\eta_2-\eta_1})\kappa_s^{-\eta_2} & \kappa_s > \kappa_0 \end{cases}, \tag{3}$$

where κ_s, the magnitude of the 3D spatial wave number, was introduced in Rino and Carrano (2018). The 3D model characterizes

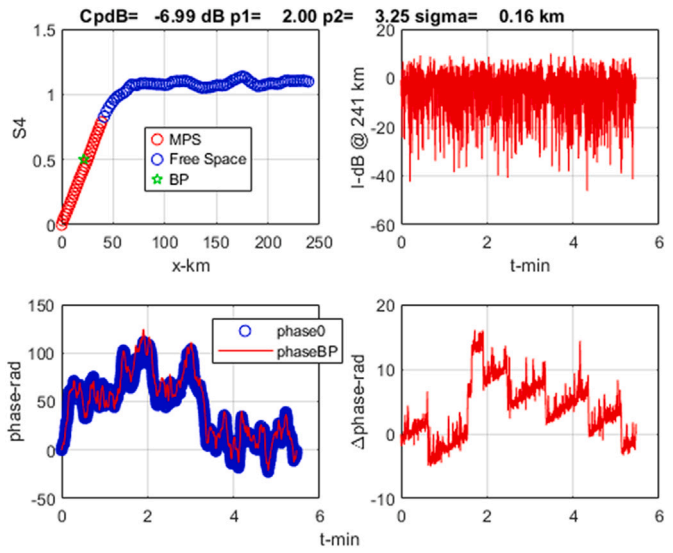

Fig. 4. PPB segment 1 summary: The upper left frame shows the MPS $S4$ evolution (red) and the subsequent free-space evolution(blue). The green pentagram identifies the BP range and $S4$. The upper right frame repeats the intensity at 142 km for reference. The lower left frame compares the initiating and BP recovered phase. The lower right frame is phase difference.

one-dimensional scans or one-dimensional measurements corresponding to translating linear path integrations exactly (Rino et al., 1981). However, because the structure is highly field aligned, stochastic variation is defined in planes that cut across field lines. It follows that propagation confined to paths that cross field lines can be characterized with two-dimensional models. Hereafter we will consider only two-dimensional structure denoted $\Delta N_e(x,y)$. There is no loss of generality if we align the x axis with the propagation direction. The y axis lies in the plane containing the propagation vector at an angle from the magnetic field direction generally referred to as the Briggs-Parkin angle. Geometrical translation details can be found in the references cited in Rino and Carrano (2018). The limitations of the model will be discussed in light of BP-IPE applications to real data.

Following the development in Rino et al. (2025), diagnostic GNSS receivers report complex signals that can be interpreted as the intensity and phase of demodulated GNSS signals embedded ideally in a white noise background. Scintillation is manifest as an imposed stochastic modulation caused by intermediate scale structure, which evolves slowly enough to be considered frozen over measurement intervals. Time series are generated by translation of the propagation path. Under the frozen-field approximation a geometry-dependent effective scan velocity converts temporal to spatial variations. The defining relation is

$$\phi(y) = 2\pi K/f_c \int_0^L \Delta N_e(x,y)dx, \tag{4}$$

where L is a layer thickness measure, $\Delta N_e(x,y)$ is a realization of the stochastic component of the electron density, f_c represents the carrier frequency,

$$K = r_e c/(2\pi) \times 10^{16}, \tag{5}$$

$r_e = 2.819740289 \times 10^{-15}$ m, and c is the vacuum velocity of light. The SDF of the projected path-integrated phase can be computed directly from (4) as

$$\Phi_\phi(\kappa_y) = \left(2\pi K L/f_c\right)^2 \int \frac{\sin^2\left(\kappa_x L/2\right)}{\left(\kappa_x L/2\right)^2} \Phi_{\Delta N_e}(\kappa_x,\kappa_y)\frac{d\kappa_x}{2\pi}, \tag{6}$$

where $\Phi_{\Delta N_e}(\kappa_x,\kappa_y)$ is the 2D SDF in the xy coordinate system. Assuming full decorrelation along the propagation path, the following relation can be used:

$$\Phi_\phi(\kappa_y) = \left(2\pi K/f_c\right)^2 L\Phi_{\Delta N_e}(0,\kappa_y). \tag{7}$$

Guided by exact relations for a single power law, we assume diagnostic measurements have the form

$$\Phi_\phi(\kappa_y) = C_p \begin{cases} \kappa_y^{-p_1}, & \kappa_y \le \kappa_0 \\ (\kappa_0^{p_2-p_1})\kappa_y^{-p_2}, & \kappa_y > \kappa_0 \end{cases} \tag{8}$$

Time-to-space conversion factors are absorbed in C_p and the break scale κ_0. Over the power-law range the power law index η is related to the corresponding one-dimensional SDF index as $p = \eta - 2$, guided again by the single power law results. Numerical integration can be use to refine estimates of 3D model parameters. Only the one-dimensional model parameters are used in this paper.

Stochastic realizations of $\phi(y)$ completely define the MPS interaction of an initiating field with an extended ionospheric region. Free-space propagation over a distance Δx is defined by the operation

$$\psi(x \pm \Delta x, y) = \int \hat{\psi}(\kappa_y; x)\left[\exp\{\mp i\left(\sqrt{1-\left(\kappa_y/k\right)^2}-1\right)\left(k\rho_F\right)^2\}\right] \times \exp\{i\kappa_y y\}d\kappa_y/(2\pi), \tag{9}$$

where $k = 2\pi f_c/c$, $\rho_F = \sqrt{\Delta x/k}$ is the Fresnel scale, and

$$\hat{\psi}(\kappa_y; x) = \int \psi(x,y)\exp\{-i\kappa_y y\}dy \tag{10}$$

is the y Fourier transform of the complex field $\psi(x,y)$. Defining the propagation step length as $\Delta x = k\rho_F^2$ anticipates the narrow-propagation-angle constraint, $\left(\kappa_y/k\right)^2 \ll 1$. The phase modification in square brackets takes the simpler form $\exp\{\pm i\left(\kappa_y\rho_F\right)^2/2\}$, which implies equivalent scintillation at distances and frequencies that preserve ρ_F. Detrending operations constrain the largest contributing measurement scales, which define locally homogeneous segments over which the summarized relations apply.

Forward propagation for MPS simulation uses the upper sign in (9); back propagation uses the lower sign. Back propagation is initiated with the measured field nominally at the propagation distance from the ionosphere penetration point. Nelder-Mede minimization (Olsson and Nelson, 1975) is applied to $\left\langle|\psi(x \pm \Delta x, y)|^2\right\rangle$. If a minimum corresponding to $S4 < 1$ is realized, the field $\psi(x-\Delta x, y)$ is accepted as an estimate of the field initiating free-space propagation. If no minimum is found or the minimum $S4$ exceeds unity, BP to the distance from the penetration point is accepted as the field initiating free-space propagation. The phase of the initiating field is extracted with a standard unwrapping algorithm IPE as described in Rino et al. (2019) is applied to the periodogram of the reconstructed phase.

The following procedure is used to generate sampled phase realizations:

$$\phi(n\Delta y) = \sum_{m=0}^{N-1} \sqrt{\Phi_\phi(m\Delta\kappa_y)\Delta\kappa_y/(2\pi)}\,\eta_m \exp\{2\pi nm/N\} \tag{11}$$

where η_m is a sequence of uncorrelated unit variance complex random variables. Formally,

$$\left\langle \eta_m \eta_{m'}^* \right\rangle = \delta(m-m'), \tag{12}$$

where $\delta(m)$ is the Kronecker delta function. From the (fast Fourier transform) FFT operation

$$\hat{\phi}(m\Delta\kappa) = \frac{1}{N}\sum_{n=0}^{N-1} \phi(n\Delta y)\exp\{-2\pi inm/N\}, \tag{13}$$

it follows that

$$\left\langle \left|\hat{\phi}(m\Delta\kappa)\right|^2 \right\rangle = \Phi_\phi(m\Delta\kappa). \tag{14}$$

The summations are implemented with FFTs sampled from $\pm\Delta\kappa$ to $\pm N\Delta\kappa/2$ where $\Delta\kappa = 2\pi/(N\Delta y)$. A $\Delta\kappa_y/(2\pi)$ scaling preserves the

Parseval relation

$$\left\langle \frac{1}{N}\sum_{n=0}^{N-1}|\phi(n\Delta y)|^2 \right\rangle = \sum_{m=0}^{N-1}\Phi_\phi(m\Delta\kappa_y)\Delta\kappa_y/(2\pi)\,. \tag{15}$$

For notational efficiency the continuous forms of the functional relations will be used with FFT evaluation implied. MPS starts with an initiating complex field. A phase realization is used to impose a phase perturbation. The modified field is propagated over an incremental distance, typically several hundred wavelengths. Exact propagation defined by (9) suppresses small-scale structure with $\kappa_y < k$, although local wavelength-scale structure can be produced, e.g. caustics. Free propagation is implemented incrementally to avoid phase discontinuities. The spatial frequency extent of the evolving PSD is a check on the small propagation angle constraint.

3. BP-IPE simulations

Diagnostic GNSS receivers typically provide 50 or 100 Hz intensity and phase data samples at L-band frequencies. The primary frequencies used for TEC computation are designated L1 and L2. As the highest frequency common to GPS and GNSS constellations, L2 MPS simulations were initiated with critically sampled ($\Delta y = \lambda/2$) phase-screen realizations followed by free propagation using (9) with $\Delta x = 600\lambda$. MPS was applied over 40 km followed by free propagation to 142 km. Phase-screen simulations in the companion paper (Rino et al., 2025) were compared to exact phase-screen theoretical results. Here MPS simulations are being used to demonstrate BP-IPE recovery of the defining structure parameters Cp, p_1, p_2 and f_0 from extended disturbed regions. EPB and PPB simulation examples were constructed by choosing measured parameters assigned to GPS Hong Kong EPB and PPB structure classes as summarized in Section 4. Realizations were initiated using 50-km phase screens with the effective scan velocity, $v_{\rm eff}$, chosen to generate 100-Hz realizations spanning 5-min segments.

Figs. 1 and 2 show intensity and phase realizations at 142 km. Green pentagrams mark the centers of each 5-min segment. The upper left frames of Figs. 3 and 4 show the associated $S4$ evolution with BP $S4$ at the minimum propagation identified by the green pentagram. The more rapid development of the PPB scintillation is a consequence of the p_1 enhancement of large-scale structure. However, for both structure classes the $S4$ at the minimum distances coincides with an $S4$ value within the structured segment. The upper right frames repeat the observation intensity for reference. The lower left frames compare the initiating phase with the reconstructed BP phase. The right frames show the differences between the initiating phase and the recovered BP phase. The EPB phase is recovered almost perfectly. The PPB phase captures the low-frequency structure with phase jumps. No attempt was made to remove the phase jumps.

Figs. 5 and 6 summarize the BP-IPE parameters extracted from each 5-min segment. Consistent with the small EPB phase errors, the initiating p_1 and p_2 parameters are recovered almost perfectly. The PPB parameters summarized in Fig. 6 show more variability and larger p_1 and p_2 errors. Nonetheless, the results show that measured $p_1 - p_2$ differences statistically favor PPB classification. Solid lines indicate the defining p_1 and p_2 values. Both scintillation classes can generate extreme scintillation with parameters that have been observed in the GNSS data as summarized in Section 4. However, statistical variation of the estimation of EPB parameters is smaller. This is expected because of coupling between C_P and p_1 estimates (Rino et al., 2014).

4. GPS BP-IPE diagnostic examples

GPS satellites are deployed in 12-h circular orbits configured to provide at least 4 favorably oriented satellites visible from any position on the earth's surface. Propagation through the ionosphere creates a delay that must be corrected, but it also provides an exceptional diagnostic capability. With support from internal funding from the University of

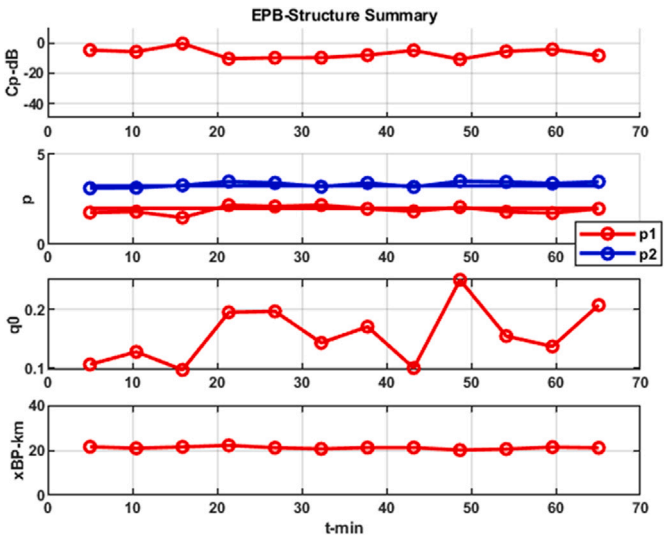

Fig. 5. Summary of measured EPB structure parameters. Blue and red lines indicate true values.

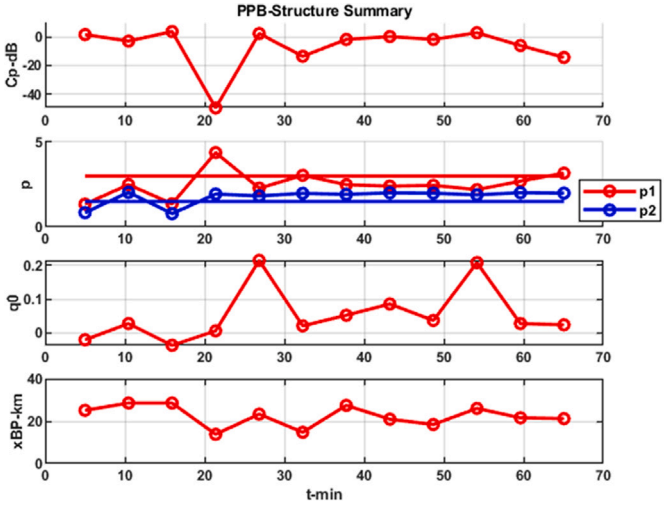

Fig. 6. Summary of measured PPB structure parameters. Blue and red lines indicate true values.

Miami Prof. Jade Morton's laboratory designed and constructed a 25 MHz multi-frequency GPS data acquisition system, which was deployed in Hong Kong hosted by Prof. George Liu from Hong Kong Polytechnic University. The system was operated from October 2013 to July 2015 with data acquisition triggered by strong scintillation. Intensity and phase data sampled at 100 Hz were made available for this study.

Following the intensity and phase processing operations summarized in Rino et al. (2025), complex scintillation records were generated to support 5-min consecutive segments for BP-IPE processing. Spectral analysis of highly disturbed intensity segments indicated that 5-min processing intervals were required to recover the large-scale structure. Fig. 7 shows representative Hong Kong L1, L2, and L5 intensity data records converted to dB SNR units (blue) with mean intensity overlaid (red). The red circles locate centers of the 5-min segments. Detrended intensity is generated by normalizing the intensity to the estimated mean.

Fig. 8 shows $S4$ scintillation index estimates for the L1 and L2 data shown in Fig. 7, which are evaluated over 5 min intervals offset by 2.5 min. Using a sliding window for $S4$ estimation is a test of the 5-min processing interval homogeneity. The L2 and L5 frequencies are

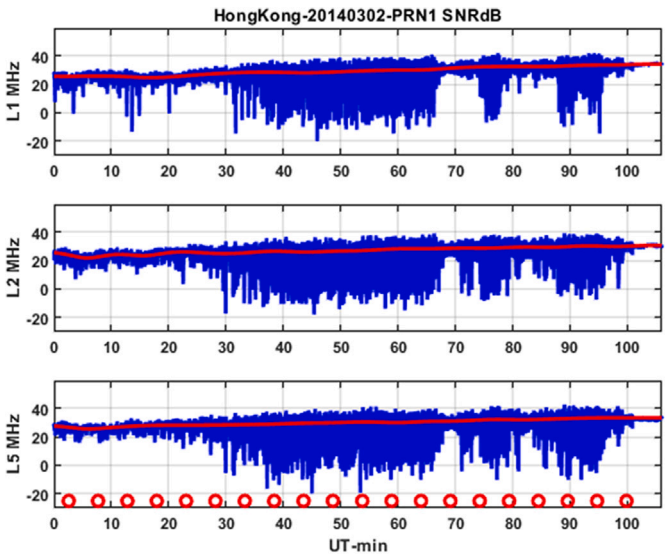

Fig. 7. Representative example of Hong Kong intensity in SNR units (blue) with mean intensity overlaid (red). Red circles mark 5-min segment centers.

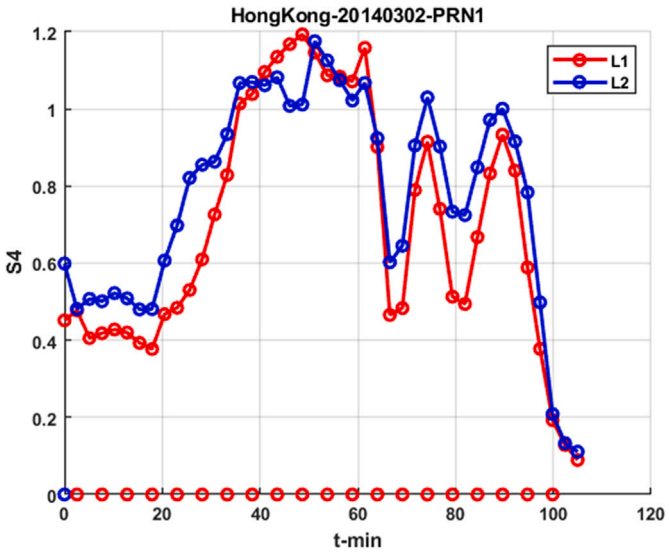

Fig. 8. Summary of Hong Kong $S4$ from L1 and L2 intensity data shown in Fig. 7.

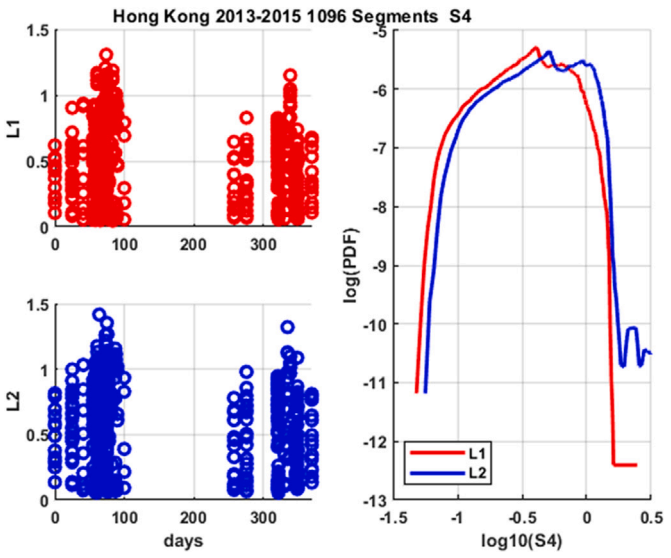

Fig. 9. Left frames summarize the measure Hong Kong L1 and L2 $S4$ segment estimates. The right frame shows the corresponding L1 and L2 $\log_{10}(S4)$ probably distributions.

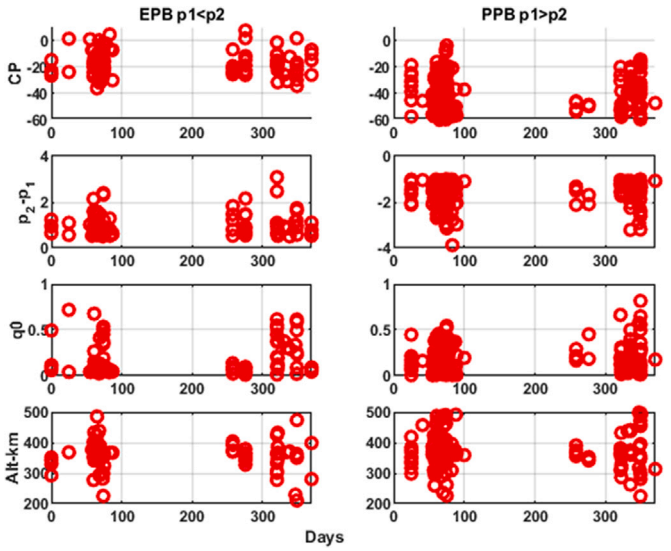

Fig. 10. Hong Kong BP-IPE parameter summaries. Left frames summarize 107 EPB segments with $q_0 = \kappa_0$. Right frames summarize 211 PPB segments. Altitude in lower frames is derived from BP propagation distance.

separated by 51 MHz, which is large enough to capture the frequency dependence of the $S4$ estimates. However, the L5 $S4$ estimates were observed to be inflated, which is attributed to an interfering signal. The L5 intensity has been excluded from further analysis. The L1 and L2 $S4$ estimates follow the expected frequency ordering with the exception of segments bracketing 50-min where the frequency order is reversed. This is attributed to strong focusing. The lower frequency passes through a strong focusing peak followed by reduction to a saturation level while the higher frequency remains in strong focusing with a higher $S4$ value. The left frames in Fig. 9 summarize the measured Hong Kong $S4$ values with the expected higher occurrence of strong scintillation in the equinox periods. The right frame shows L1 and L2 $S4$ distributions of $\log_{10}(S4)$. The distributions are consistent with the overall frequency dependence but obscure strong focusing.

A complex scintillation estimate was constructed by imposing the extracted phase after removal of an 8th order polynomial approximation onto the detrended scintillation intensity. The preprocessing operations used to generate the complex signal represent the ideal model simulations in a background of white noise. Unmodified BP-IP processing operations were applied to 5-min segments of the L2 Hong Kong data. BP minimization was initiated with the propagation distance to the ionosphere penetration point at 350 km. BP-IPE processing was applied to 1159 segments. An estimate of the true altitude of the ionosphere penetration point was computed from the known source-to-receiver propagation distance and the BP propagation distance. Segments with BP altitudes outside 200 to 500 km were discarded as BP failures. Of the surviving 719 segments, 107 with $p_2 - p_1 > 0.5$ were classified EPB, 201 segments with $p_1 - p_2 > 1$ were classified PPB. The remaining 401 segments could not be classified definitively. The simulation parameters EPB $p_1 = 2$, $p_2 = 3.5$ and PPB $p_1 = 3$, $p_2 = 1.5$ used in Section 2 are representative values. Fig. 10 summarizes the EPB and PPB segment parameters separately; C_p in the

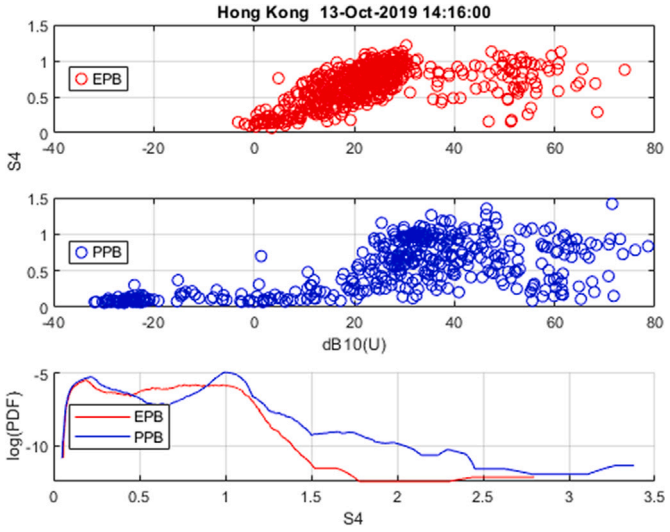

Fig. 11. Upper frames show $S4$ versus U scatter diagrams for EPB and PPB segments as indicated. Lower frame shows corresponding $S4$ probability distributions.

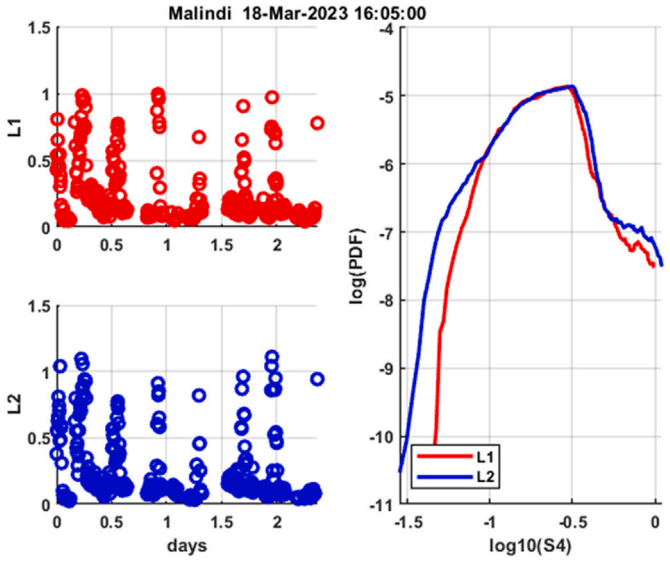

Fig. 12. Measured PPB segment $S4$ values (upper frames) and distribution from data recorded at Malindi 18-Mar-2019 20:45:02.

top frames, EPB $p_2 - p_1 > 1$ and PPB $p_1 - p_2$ in the second frames, q_0 in the third frames, and the estimated altitude in the fourth frames.

Although theoretical results were not used to estimate structure parameters, the estimated structure parameters can be used to predict the theoretical intensity SDF and $S4$ values. Predicted and measured SDFs could then be compared to validate the IPE parameters. However, a more efficient check on the integrity of the IPE parameters is to verify that the independently measured $S4$ values are ordered by the universal strength parameter

$$U = C_P \begin{cases} \rho_F^{p_1-1} & \text{for } \mu_0 \le 1 \\ \rho_F^{p_2-1}\kappa_0^{p_1-p_2} & \text{for } \mu_0 \le 1 \end{cases}, \tag{16}$$

where $\mu_0 = \kappa_0\rho_F$, Carrano and Rino (2016). The upper frames of Fig. 11 show, respectively, $S4$ versus U scatter diagrams with U computed from (16) using the measured structure parameters. Allowing for statistical uncertainty the predicted U parameter orders the intensity scintillation for both EPB and PPB segments. The $S4$ occurrence probabilities are shown in the lower frame. Extreme $S4$ values occur within EPB and PPB structures. However, PPB extreme $S4$ values are more likely, reflecting the impact of enhanced large-scale structure. The population of small PPB $S4$ values may be a separate population of weak structure consistent with the two peaks shown in the lower frame of Fig. 11.

Scintillation data managed by the Italian Istituto Nazionale di Geofisica e Vulcanologia (INGV) were utilized to complement the analysis. These data were collected by Ionospheric Scintillation Monitoring Receivers (ISMRs) situated in Lampedusa (Southern Italy), which covers the lower Western Mediterranean sector (Pica et al., 2025). Additional data were collected from an ISMR receiver developed under the New Observatory for Real-time Ionospheric Sounding over Kenya (NORISK, https://norisk.rm.ingv.it/) project. The receiver is located at the Luigi Broglio Malindi Space Center in Kenya, which covers the southern crest of the equatorial ionospheric anomaly (Cesaroni et al., 2025). Both ISMRs are Septentrio PolaRx5S receivers, representing an advancement from the PolaRxS (Bougard et al., 2011).

Consistent with Spogli et al. (2024) and despite its limited field of view, the scintillation enhancements recorded at Lampedusa are attributable to the spill-over of EPB irregularities rather than local multipath. Selected satellites from all four GNSS constellations reveal that intense S4 signatures were not confined to the horizon but occurred simultaneously across a wide range of elevation angles, extending up to 50° (not shown). This simultaneous detection across disparate viewing geometries is consistent with the interception of vertical EPB sidewalls, confirming the usability of the Lampedusa data set for characterizing these storm-induced irregularities.

Identical BP-IPE processing and data editing was applied to Malindi and Lampedusa 5-min L2 data segments sampled at 50 Hz. Although the data segments processed were smaller in number, a fraction comparable to the Hong Kong data produced parameter estimates. Figs. 12 and 13, which can be compared directly to Fig. 9 show strikingly similar extreme scintillation occurrence and distributions over two-day periods. The Lampedusa and Malindi stations are observing structure respectively from north and south of the equatorial region where equatorial bubbles are developing. Figure 9 in Spogli et al. (2024) summarizes the Lampedusa Gannon Storm activity, which is attributed to intercepting developed equatorial bubbles. Figs. 14 and 15, which can be compared directly to Fig. 10 show that the segment structure is predominately PPB. This may be due to the more varied multiple GNSS satellite multiple geometries reflected in the altitude variation. The identically repeated GPS orbits favor the cross-field geometry that captures the EPB signature.

5. Summary and conclusions

A new diagnostic procedure that exploits BP to characterize the ionospheric structure that causes scintillation has been described and validated with MPS simulations. BP-IPE processing is implemented with standard PSD and minimization procedures that could be executed in near-real-time. Additionally, as extreme scintillation in the title of the paper implies, BP-IPE processing can be used effectively as long as the diagnostic receiver is maintaining lock. Moreover, the model parameters and structure altitude can be estimated without recourse to theoretical results.

Supplementing standard $S4$, σ_ϕ, and rate of total intensity change (ROTI) parameters with C_P, p_1, p_2, f_0, and propagation distance would allow direct model predictions of the standard parameters in addition to characterizing the structure quantitatively. The interpretation of IPE parameters is constrained to highly elongated structure that can be approximated with 2D propagation, which also constrains occultation BP applications. Regarding geometric constraints, routinely observed near field-aligned propagation is not precluded. However, quantitative

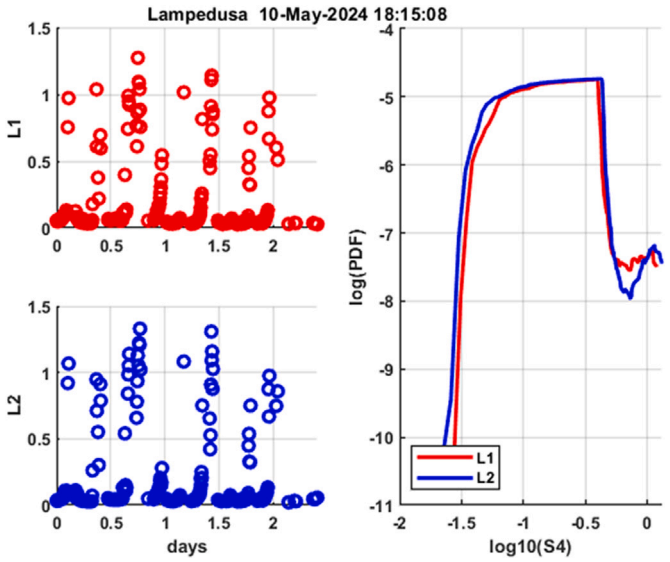

Fig. 13. Measured PPB segment $S4$ values (upper frames) and distribution from data recorded at Lampedusa 10-May-2019 16:00:00.

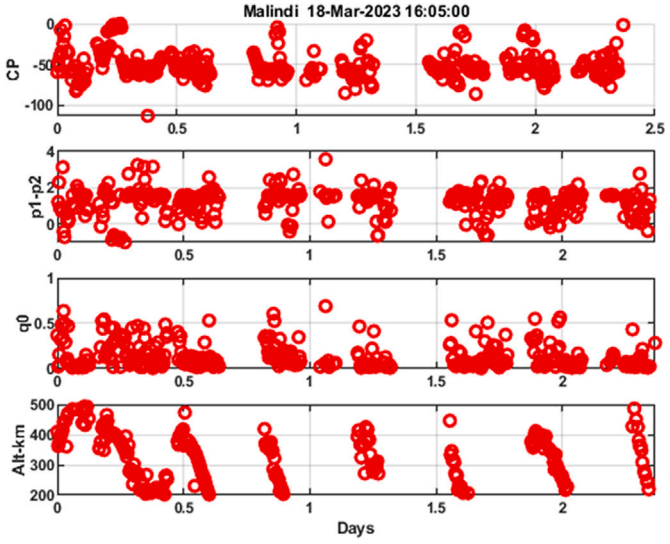

Fig. 14. BP-IPP parameters from Malandi data. The second frame shows $p_1 - p_2$ with positive values identified as PPB signatures and $q_0 = \kappa_0$. Altitude in lower frames is derived from BP propagation distance.

interpretation of inhomogeneous and/or truncated segments is more demanding.

To illustrate the limitations of the standard scintillation measures the σ_ϕ, and ROTI estimates over 5-min processing intervals were calculated using the MPS EPB and PPB simulations summarized in Section 2. ROTI is expressed in radians per second rather than TEC per second units. From the standard parameters alone the large increase in σ_ϕ suggest but does not characterize underlying structure differences.

EPB

Diagnostic	mean	std
$S4$	0.84	0.03
σ_ϕ	12.65 rad	3.38 rad
$ROTI - 1$ min	0.19 rad/s	0.08 rad/s

PPB

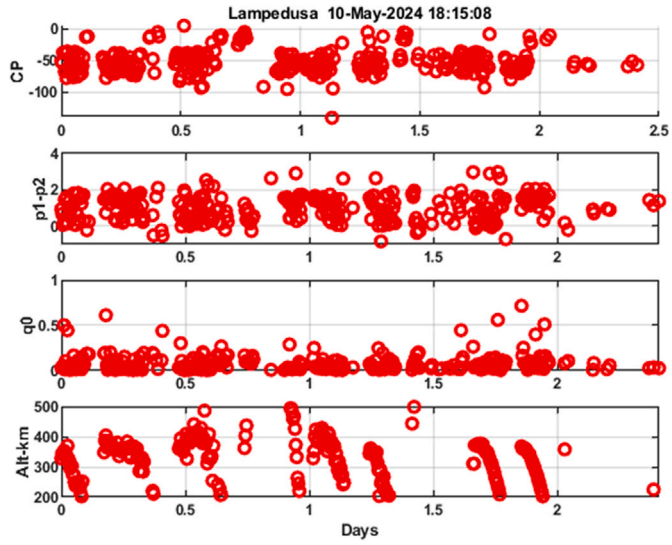

Fig. 15. BP-IPP parameters from Lampedusa data. The second frame shows $p_1 - p_2$ with positive values identified as PPB signatures and with $q_0 = \kappa_0$. Altitude in lower frames is derived from BP propagation distance.

Diagnostic	mean	std
$S4$	1.00	0.01
σ_ϕ	87.30 rad	33.90 rad
$ROTI - 1$ min	0.94 rad/s	0.44 rad/s

With regard to electron density structure associated with EPB phenomena, it is informative to review the published results that led to the two-component model hypothesis. We cited early rocket measurements of equatorial plasma bubbles (Rino et al., 1981). Analysis of in-situ satellite data from the Atmospheric Explorer E (Basu et al., 1983) and C/NOFS satellites (Rino et al., 2014) confirmed the EPB structure. Additionally, the frequency dependence implied by the EPB structure reconciled the unexpected occurrence of communication system S-Band scintillation (Craft and Westerlund, 1972; Franke et al., 1984). Further support came from physics-based high-resolution simulations of the evolution of equatorial plasma bubbles (Yokoyama, 2017). A representative EPB structure evolution was deduced from simulations of an isolated plasma bubble. Definitive EPB structure is established when the plasma bubble penetrates F-region peak density. Late phase EPB structure approaches a single power law [See Figures 3 through 6 in Rino et al. (2023)]. There was no indication of enhanced large-scale structure.

The Hong Kong BP-IPE analysis shows larger numbers of segments with EPB structure with extreme scintillation segments within each structure class. The Malindi and Lampedusa results were predominantly PPB with extreme scintillation segments. The results suggest a more complicated 3D structure variation than the purely geometrical variation predicted by structure with contours of constant correlation or spectral intensity characterized by stretched ellipsoidal contours. Evidently, the defining structure is changing as it is being mapped along field lines. Analysis is being pursued to understand the observed structure variation.

CRediT authorship contribution statement

Charles Rino: Writing – review & editing, Writing – original draft, Validation, Investigation, Formal analysis, Conceptualization. **Charles Carrano:** Validation, Formal analysis, Conceptualization. **Dmytro Vasylyev:** Writing – review & editing, Validation, Conceptualization. **Luca Spogli:** Investigation, Data curation. **Theodore Beach:** Conceptualization. **Yu Morton:** Writing – review & editing, Data curation. **Keith Groves:** Supervision.

Declaration of competing interest

The authors declare that they have no known competing financial interests or personal relationships that could have appeared to influence the work reported in this paper.

Acknowledgments

The authors thank Claudio Cesaroni and Emanuele Pica for their help with the ISMR data from Lampedusa and in Malindi. The ISMR in Malindi has been established as part of the New Observatory for Real-time Ionospheric Sounding over Kenya (NORISK, https://norisk.rm.ingv.it/) project, carried out in the framework agreement between the Italian Space Agency (ASI) and the Istituto Nazionale di Geofisica e Vulcanologia (INGV). ISMR data from Lampedusa and Malindi are available at www.eswua.ingv.it: https://doi.org/10.13127/ESWUA/GNSS Upper Atmosphere Physics and Radiopropagation Working Group: Electronic Space Weather Upper Atmosphere Database (eSWua)-GNSS Scintillation Data, Version 1.0. Istituto Nazionale di Geofisica e Vulcanologia (INGV) August 1, 2020. The Hong Kong GPS data will be made available upon request.

Data availability

Data will be made available on request.

References

Basu, S.S.B., McClure, J.P., Hanson, W.B., Whitney, H.E., 1983. High resolution topside in situ data of electron densities and VHF/GHZ scintillations in the equatorial region. J. Geophys. Res. Space Phys. 88, 403–415. http://dx.doi.org/10.1029/JA088iA01p00403.

Bougard, B., Sleewaegen, J.M., Spogli, L., Veettil, S.V., Monico, J.F., 2011. CIGALA: Challenging the solar maximum in Brazil with PolaRxS. In: Proceedings of the 24th International Technical Meeting of the Satellite Division of the Institute of Navigation. Ion GNSS 2011, pp. 2572–2579.

Breitsch, B., Morton, Y.T., Rino, C., Xu, D., 2020. GNSS carrier phase cycle slips due to diffractive ionosphere scintillation simulation and characterization. IEEE Trans. Aerosp. Electron. Syst. 56, 3632–3644. http://dx.doi.org/10.1109/TAES.2020.2979025.

Carrano, C., Rino, C., 2016. A theory of scintillation for two-component power law irregularity spectra: Overview and numerical results. Radio Sci. 51, 789–813. http://dx.doi.org/10.1002/2015RS005903.

Cesaroni, C., Pezzopane, M., Zuccheretti, E., Pica, E., Spogli, L., Okoh, D., Pignalberi, A., Olwendo, J., Alfonsi, L., Marcocci, C., Romano, V., Imam, R., De Franceschi, G., Nava, B., Habarulema, J.B., Santilli, G., Di Cecco, A., Munzer, J., 2025. Establishing the first ionospheric observatory in Kenya: Early results from the NORISK project. Adv. Space Res. 75, 4698–4713. http://dx.doi.org/10.1016/j.asr.2025.01.051.

Craft, H.D., Westerlund, L.H., 1972. Scintillation at 4 and 6 GHZ caused by the ionosphere. In: AIAA 10th Aerospace Sciences Meeting. Vol. 72–179, San Diego, CA, pp. 1–6. http://dx.doi.org/10.2514/6.1972-179.

Franke, S.J., Liu, C.H., Fang, D.J., 1984. Multifrequency study of ionospheric scintillation at Ascension Island. Radio Sci. 19, 695–706. http://dx.doi.org/10.1029/RS019i003p00695.

Ludwig-Barbosa, V., Rasch, J., Sievert, T., Carlström, A., Pettersson, M.I., Vu, V.T., Christensen, J., 2023. Detection and localization of F-layer ionospheric irregularities with the back-propagation method along the radio occultation ray path. Atmospheric Meas. Technol. 16, 1849–1864. http://dx.doi.org/10.5194/amt-16-1849-2023.

Olsson, D.M., Nelson, L.S., 1975. The Nelder-Mead simplex procedure for function minimization. TECHNOMETRICS 17, 45–51.

Pica, E., Spogli, L., Cesaroni, C., Alfonsi, L., Haralambous, H., Vallianatos, F., De Franceschi, G., Romano, V., Marcocci, C., 2025. Assessing the ionospheric scintillations occurrence on L-band in the southern Mediterranean sector. Adv. Space Res. 75, 837–855. http://dx.doi.org/10.1016/j.asr.2024.10.032.

Rino, C.L., Carrano, C.S., 2018. On the characterization of intermediate-scale ionospheric structure. Radio Sci. 53, 1316–1327. http://dx.doi.org/10.1029/2018RS006709.

Rino, C.L., Carrano, C.S., Roddy, P., 2014. Wavelet-based analysis and power law classification of C/NOFS high-resolution electron density data. Radio Sci. 49, 680–688. http://dx.doi.org/10.1002/2013RS005272.

Rino, C., Carrano, C., Vasylyev, D., Beach, T., Breitsch, B., Morton, Y., Groves, K., 2025. On phase screen models for scintillation diagnostics. Radio Sci. 60, e2024RS008204. http://dx.doi.org/10.1029/2024RS008204.

Rino, C., Morton, Y., Breitsch, B., Carrano, C., 2019. Stochastic TEC structure characterization. J. Geophys. Res. Space Phys. 124, 10571–10579. http://dx.doi.org/10.1029/2019JA026958.

Rino, C.L., Tsunoda, R.T., Petriceks, J., Livingston, R.C., Kelley, M.C., Baker, K.D., 1981. Simultaneous rocket-borne beacon and in situ measurements of equatorial spread F – Intermediate wavelength results. J. Geophys. Res. Space Phys. 86, 2411–2420. http://dx.doi.org/10.1029/JA086iA04p02411.

Rino, C., Yokoyama, T., Carrano, C., 2023. A three dimensional stochastic structure model derived from high resolution isolated equatorial plasma bubble simulations. Earth, Planets Space 75 (64), http://dx.doi.org/10.1186/s40623-023-01823-6.

Spogli, L., Alberti, T., Bagiacchi, P., Cafarella, L., Cesaroni, C., Cianchini, G., Coco, I., Di Mauro D, D., Ghidoni, R., Giannattasio, F., Ippolito, A., Marcocci, C., Pezzopane, M., Pica, E., Pignalberi, A., Perrone, L., Romano, V., Sabbagh, D., Scotto, C., Spadoni, S., Tozzi, R., Viola, M., 2024. The effects of the May 2024 Mothers Day superstorm over the Mediterranean sector. Ann. Geophys. 67, PA218. http://dx.doi.org/10.4401/ag-9117.

Yokoyama, T., 2017. A review on the numerical simulation of equatorial plasma bubbles toward scintillation evaluation and forecasting. Prog. Earth Planet Sci. 4 (37), http://dx.doi.org/10.1186/s40645-017-0153-6.